ACS Catalysis
Letter
pubs.acs.org/acscatalysis

Facet-Dependent Catalytic Activities of Au Nanoparticles Enclosed by High-Index Facets

Qingfeng Zhang and Hui Wang*

Department of Chemistry and Biochemistry, University of South Carolina, 631 Sumter Street, Columbia, South Carolina 29208, United States

Supporting Information

ABSTRACT: We employed surface-enhanced Raman scattering as a noninvasive *in situ* spectroscopic tool to quantitatively study the intrinsic facet-dependent catalytic activities of colloidal subwavelength Au nanoparticles enclosed by various types of well-defined high-index facets using the catalytic hydrogenation of 4-nitrothiophenol as a model reaction. Our results provide compelling experimental evidence on the crucial roles of undercoordinated surface atoms in Au-based heterogeneous catalysis and shed light on the underlying relationship between the atomic-level surface structures and the intrinsic catalytic activities of Au nanocatalysts.

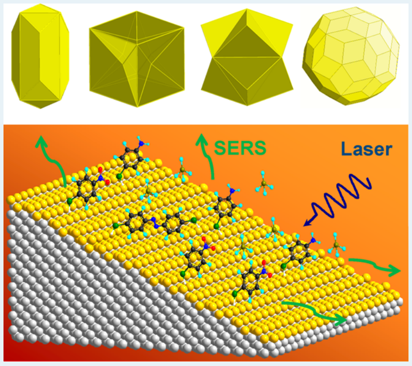

KEYWORDS: *nanocatalysis, high-index facets, Au nanoparticles, plasmon resonances, surface-enhanced Raman spectroscopy*

Intriguing nanoscale effects are broadly involved in heterogeneous catalysis, which can probably be best manifested by the size-dependent catalytic activities observed on Au nanoparticles (NPs).[1−6] In striking contrast to their mesoscopic and bulk counterparts that are chemically inert, sub-5 nm Au NPs supported on high-surface-area oxide materials exhibit exceptionally high catalytic activities toward a series of oxidation and hydrogenation reactions under mild conditions.[1−10] It is ubiquitously believed that the undercoordinated surface atoms located at the particle corners and edges, whose abundance increases significantly as the particle size shrinks down to the sub-5 nm size regime, provide a key contribution to the remarkable catalytic activities of small Au NPs.[6,11−13] Interestingly, free-standing dealloyed nanoporous Au membranes also possess highly curved local surface structures with high fraction of undercoordinated surface atoms and thus exhibit similar catalytic activities as the oxide-supported sub-5 nm Au NPs even though their nanopores and ligaments are far beyond 5 nm in size.[14−17] Building detailed, quantitative correlation between the surface structures and the intrinsic catalytic activities of Au, however, has been extremely challenging due to the structural and compositional complexity of these nanocatalyst systems. Both the oxide supports in contact with the Au NPs[18,19] and the residual Ag present in the dealloyed Au nanoporous membranes[17,20] have been found to have strong synergistic effects on the overall catalytic competence of the materials. In addition, the lack of precise control over the atomic-level surface structures of these Au nanocatalysts remains a substantial obstacle to the elucidation of detailed structure−property relationship that underpins the Au-based heterogeneous catalysis.

Here we endeavor to gain quantitative insights into the intrinsic facet-dependent catalytic activities of Au NPs using the room temperature catalytic hydrogenation of 4-nitrothiophenol (4-NTP) as a model reaction. We are particularly interested in the catalytic activities of high-index facets of Au because high-index facets are open surface structures with high densities of coordinatively unsaturated atoms at the surface steps and kinks and thereby exhibit dramatically enhanced catalytic activities toward a variety of chemical and electrochemical reactions in comparison to the close-packed low-index facets.[21−23] In this work, Au elongated tetrahexahedral (ETHH), concave cubic (CC), and trisoctahedral (TOH) NPs are selected as three representative model nanostructures each of which is exclusively enclosed by one specific type of high-index facets. The Au ETHH, CC, and TOH NPs are all in the subwavelength size regime with well-defined facets significantly larger than 5 nm in size, ensuring that the catalytic activities are essentially determined by the characteristic distribution of undercoordinated surface atoms on each type of facets rather than those at the particle corners and edges. Distinct from the sub-5 nm Au NPs whose plasmon resonances are vanishingly weak, subwavelength Au ETHH, CC, and TOH NPs exhibit appealing plasmonic properties that enable the use of surface-enhanced Raman scattering (SERS) as a unique noninvasive ultrasensitive spectroscopic tool to precisely monitor, in real time, the molecular transformations occurring at the molecule-catalyst interfaces.[24−28]

Received: August 8, 2014
Published: October 10, 2014

dx.doi.org/10.1021/cs501445h | *ACS Catal.* 2014, 4, 4027−4033

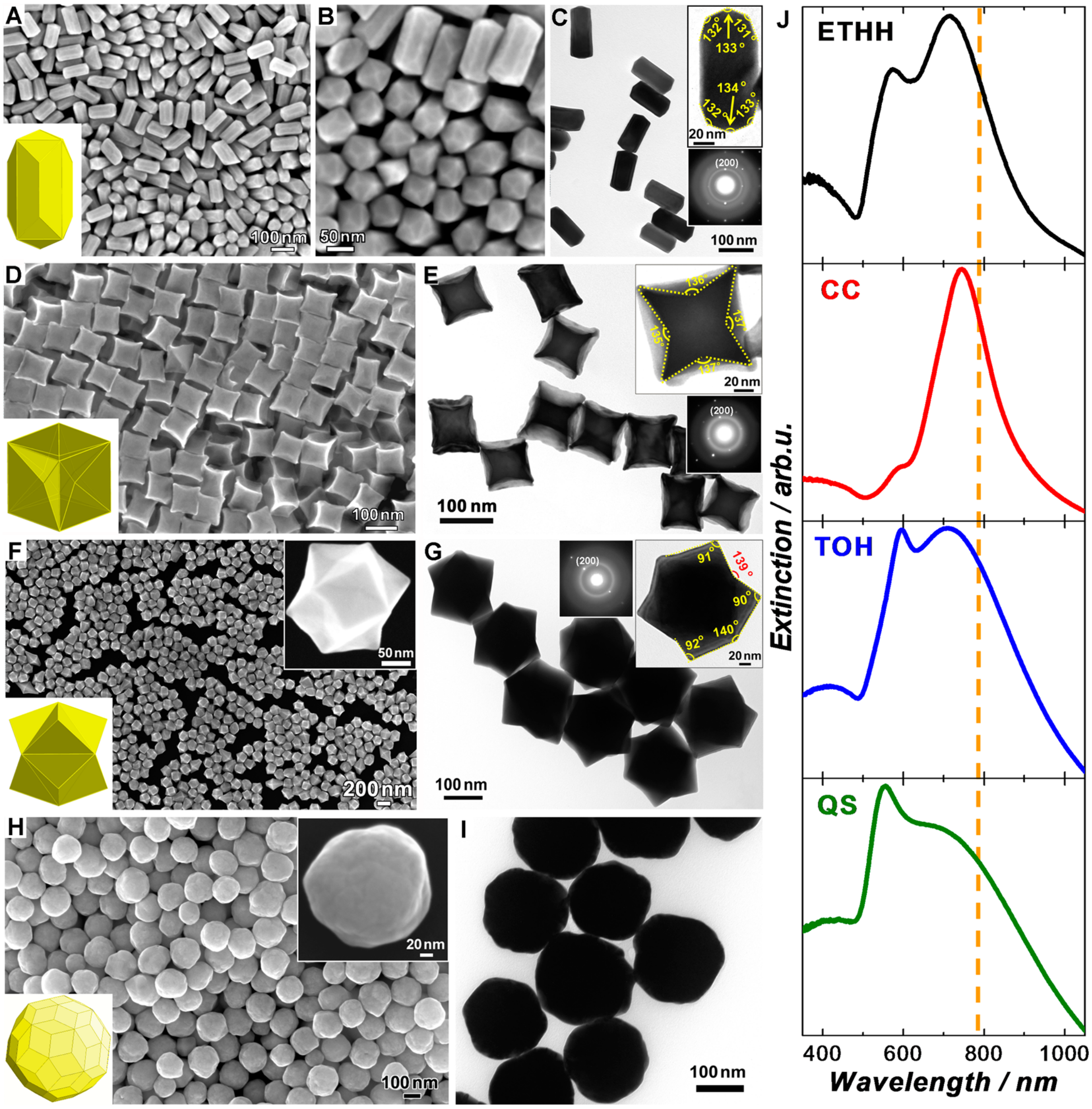

Figure 1. Structures of Au ETHH, CC, TOH, and QS NPs. (A, B) SEM images of Au ETHH NPs. The inset of panel A shows the geometric model of an ETHH NP. (C) TEM images of Au ETHH NPs (insets: high-magnification TEM image and SAED pattern of an individual Au ETHH NP viewed along the [001] projection). (D) SEM image of Au CC NPs (inset: geometric model of a CC NP). (E) TEM image of Au CC NPs (insets: high-magnification TEM image and SAED pattern of an individual Au CC NP viewed along the [001] projection). (F) SEM image of Au TOH NPs (upright inset: high-magnification SEM image of an individual Au TOH NP; bottom left inset: geometric model of a TOH NP). (G) TEM image of Au TOH NPs (insets: high-magnification TEM image and SAED pattern of an individual Au TOH NP viewed along the [011] projection). (H) SEM image of Au QS NPs (upright inset: high-magnification SEM image of an individual Au QS NP; bottom left inset: geometry model of a QS NP). (I) TEM image of Au QS NPs. (J) Optical extinction spectra of colloidal suspensions of Au ETHH, CC, TOH, and QS NPs. The vertical dashed line indicates the wavelength (785 nm) of the excitation laser for SERS measurements.

For Au NPs with face-centered cubic (fcc) crystalline structures, the surface energies of the low-index {111} and {100} facets are significantly lower than the {110} and other high-index facets.[22,29] As a consequence, Au nanoparticles enclosed by the low energy facets, such as nanocubes ({100} facets), nano-octahedra ({111} facets), and multitwined quasi-spherical NPs ({111} and {100} facets), represent the most stable nanoparticle geometries that are experimentally realizable. Although synthetically more challenging, polyhedral Au NPs enclosed by various types of high-index facets have been fabricated through facet-controlled nanocrystal growth processes.[30−34] Here we adopted a versatile seed-mediated growth method to fabricate Au ETHH, CC, and TOH NPs in a shape-selective and size-controlled manner. As shown by the scanning electron microscopy (SEM) and transmission electron microscopy (TEM) images in Figure 1, the as-fabricated Au ETHH, CC, and TOH NPs all exhibited high monodispersity in terms of both particle sizes and morphologies.

An ETHH NP is derived geometrically from a nanocuboid enclosed by 6 {100} facets upon introduction of surface convexity (Figures 1A-C). The Au ETHH NPs displayed different projected contours in the TEM images when they

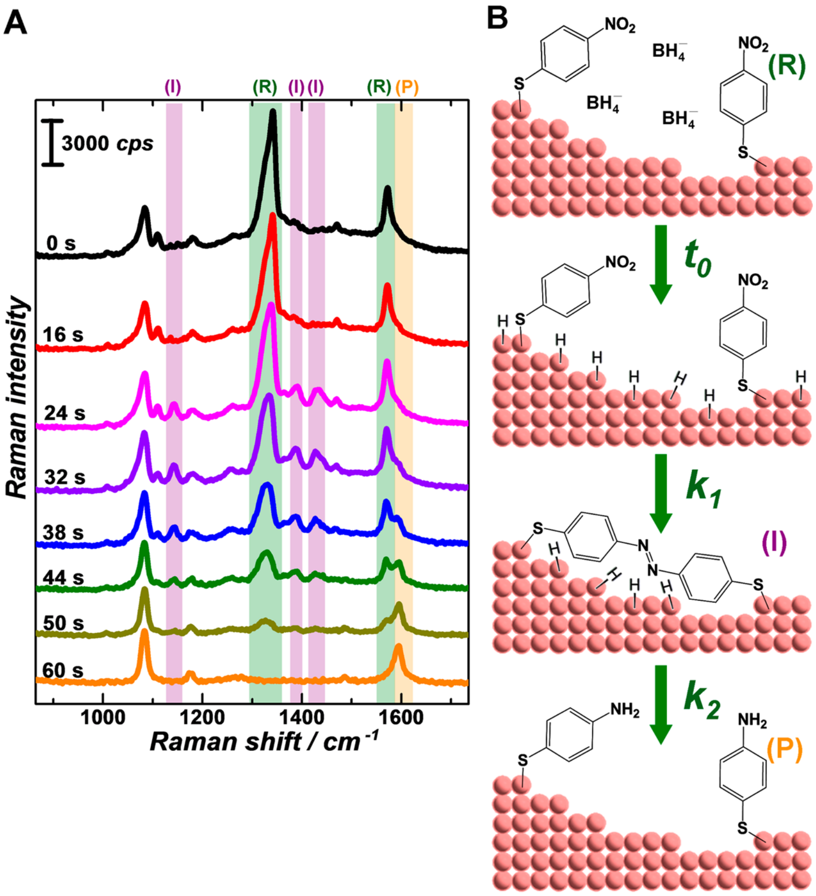

Figure 2. Monitoring surface-catalyzed reactions on Au CC NPs by time-resolved SERS. (A) Representative SERS spectra collected from 4-NTP adsorbed on the surfaces of Au CC NPs at different reaction times of 0, 16, 24, 32, 38, 44, 50, and 60 s after introducing NaBH$_4$. The spectra were offset for clarity. (B) Schematic illustration of the reduction of surface-adsorbed 4-NTP (reactant, R) to DMAB (intermediate, I) and finally to 4-ATP (product, P).

were orientated differently on the TEM grid and the orientation-dependent projection contours fit the geometric model very well (Figure S1 in the Supporting Information). The insets of Figure 1C show the TEM image and selected area electron diffraction (SAED) pattern of one ETHH NP imaged with the electron beam projected along the [001] zone axis. Under this orientation, 8 out of the 24 facets became parallel to the projection direction, allowing us to measure the characteristic dihedral angles as labeled in the figure. This result indicates that each ETHH NP is enclosed by 24 high-index {730} facets.[31] A CC NP is geometrically derived by introducing tetragonal indentation to each {100} facet of a nanocube (Figures 1D and 1E). Each CC NP appeared darker in the interior regions than in the edge regions and displayed orientation-dependent projection profiles and contrast in the TEM images (Figure S2 in the Supporting Information). The insets of Figure 1E show the TEM image and SAED pattern of one CC NP imaged with the electron beam projected along the [001] zone axis. While the Au CC NP appeared to have a cubic morphological outline under this projection, the degree of indentation could be characterized by measuring the indentation angles (the dihedral angle between indented facets) based on the different contrast in the TEM image. As marked in the figure, the indentation angles were measured to be 136 ± 1°, indicating that each Au CC NP is enclosed by 24 high-index {520} facets. The as-fabricated Au CC NPs exhibited a higher degree of indentation in comparison to the Au CC NPs with {720} facets (indentation angle of 148°) previously reported by Mirkin and co-workers.[33] A TOH NP is obtained by creating a trigonal pyramid on each triangular {111} facet of a nano-octahedron (Figures 1F and 1G). The insets of Figure 1G show the TEM image and the SAED pattern of one Au TOH NP projected from the [011] zone axis. Under this orientation, 4 out of the 24 facets of the TOH NP were projected edge-on, and the exposed facets were determined to be {221}[32] through analysis of the characteristic projection angles marked in the figure. The TEM projection outlines of individual TOH NPs with various orientations are shown in Figure S3 in the Supporting Information. The single-crystalline Au ETHH, CC, and TOH NPs provided unique NP systems for us to quantitatively compare the catalytic activities of three types of high-index facets, {730}, {520}, and {221} facets. We also fabricated multitwinned Au quasi-spherical (QS) NPs enclosed by {100} and {111} facets (Figures 1H and 1I) to further compare the catalytic activities of the high-index facets with those of the low-index facets.

Using the seed-mediated growth method, the size of the NPs can be precisely controlled for each geometry by adjusting the amount of Au seeds added into the reaction mixtures. The Au ETHH, CC, and TOH NPs all exhibited size-dependent plasmonic tunability, allowing us to fine-tune, through deliberate size control, their plasmon resonances with respect to the excitation laser wavelength to achieve optimal SERS enhancements on individual NPs. While on-resonance

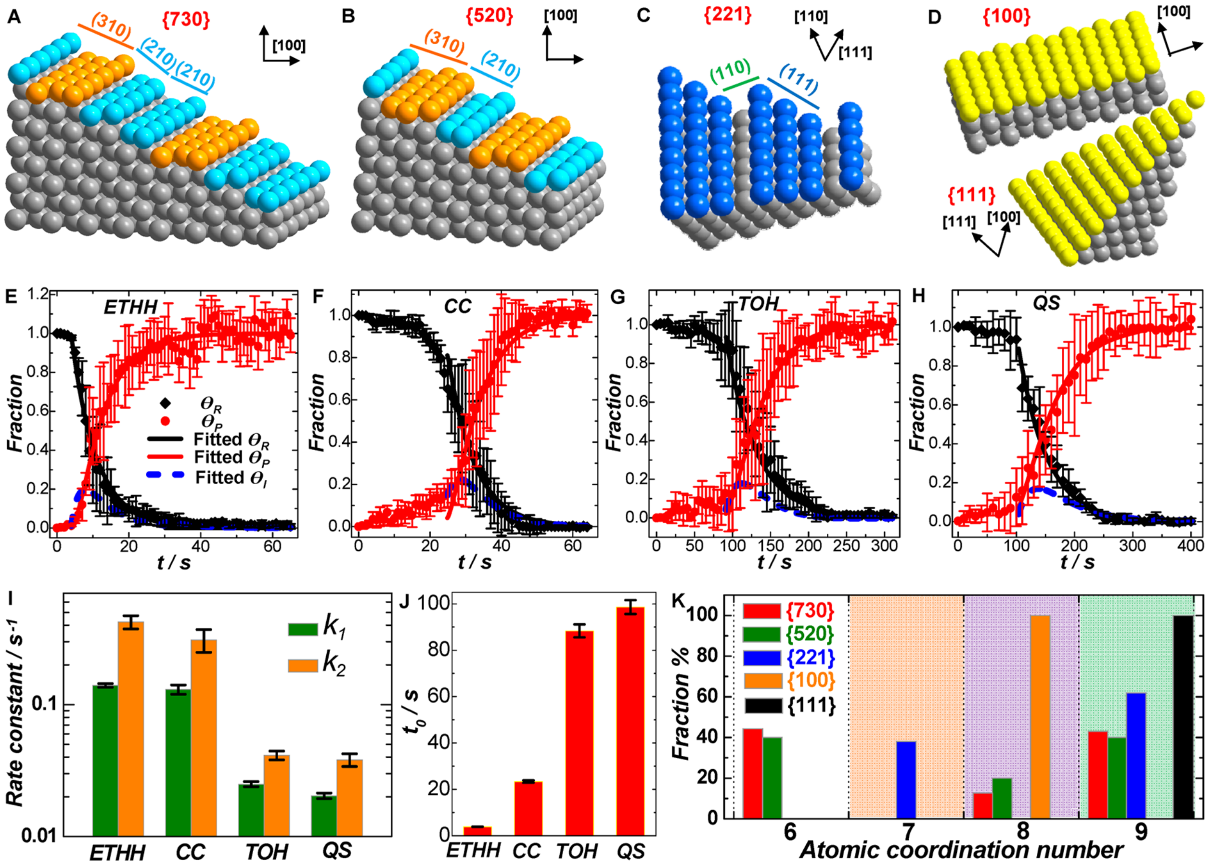

Figure 3. Facet-dependent catalytic activities of Au NPs. Schemes of the atomic level surface structures of (A) the {730} facet of Au ETHH NPs, (B) the {520} facet of Au CC NPs, (C) the {221} facet of Au TOH NPs, and (D) the {111} and {100} facets of Au QS NPs. (E-H) Fraction of reactant (θ_R), intermediate (θ_I), and product (θ_P) as a function of reaction time during the reactions catalyzed by Au (E) ETHH, (F) CC, (G) TOH, and (H) QS NPs. The error bars show the standard deviations obtained from five experimental runs. The results of the least-squares fitting are shown as solid curves for the reactants and products. The fitted results for the intermediate trajectories are shown as dash blue curves. Panels E-H share the same legends in Panel E. (I) The comparison of rate constants, k_1 and k_2, of the two-step surface reactions on Au ETHH, CC, TOH, and QS nanoparticles. (J) The comparison of induction time, t_0, of the reactions on Au ETHH, CC, TOH, and QS NPs. (K) Fraction of the coordination numbers of the surface atoms for the {730} (ETHH), {520} (CC), {221} (TOH), and {111}/{100} (QS) facets.

excitations typically generate higher Raman enhancements than the off-resonance excitations,[35] the far-field plasmon resonance bands do not overlap exactly with the wavelengths at which the largest near-field enhancements are achieved. It has been demonstrated both theoretically and experimentally on various metallic nanostructures that the maximum near-field enhancements occurred at longer wavelengths relative to the far-field extinction peaks.[36−40] With this key design principle in mind, the characteristic plasmon resonances of the Au ETHH, CC, TOH, and QS NPs were all tuned to be within the same spectral region that was blue-shifted by 35 to 70 nm in wavelength with respect to the excitation laser (785 nm). As shown in Figure 1J, subwavelength Au ETHH, CC, TOH, and QS NPs exhibited their own geometry-dependent plasmonic characteristics. Due to the rod-like anisotropic structures, colloidal Au ETHH NPs exhibited a longitudinal and a transverse plasmon bands at ∼720 nm and ∼570 nm, respectively. Au CC NPs displayed a well-define dipole plasmon resonance band at ∼750 nm and a quadrupole shoulder at ∼590 nm. Due to the phase retardation effects,[41] the dipole plasmon bands of TOH and QS NPs were both significantly broadened, and sharper quadrupole bands emerged at shorter wavelengths relative to the dipole bands.

We used SERS to monitor, in real time, the catalytic hydrogenation of 4-NTP adsorbed on the surfaces of the Au ETHH, CC, TOH, and QS NPs. Colloidal suspensions of the NPs were first incubated with ethanolic solution of 4-NTP overnight to undergo a ligand exchange process through which saturated self-assembled monolayers (SAMs) of 4-NTP were immobilized on the NP surfaces. The 4-NTP-coated NPs were redispersed as colloidal suspensions in water, and the catalytic reactions were initiated upon introduction of $NaBH_4$ at room temperature (298 K). Figure 2A shows the evolution of SERS spectra upon exposure of 4-NTP-coated Au CC NPs to 100 mM $NaBH_4$. 4-NTP showed three characteristic SERS bands at 1076, 1338, and 1571 cm^{-1}, respectively.[26−28] Upon exposure to $NaBH_4$, there was an induction time (t_0) of ∼20 s during which the SERS features of 4-NTP remained unchanged. This induction time is most likely due to the formation of active surface hydrogen species upon adsorption of borohydride ions onto the Au surfaces.[42] Only when the concentration of the surface hydrogen species was built up to a certain threshold value was the hydrogenation of 4-NTP initiated. As the reaction proceeded, the peak intensities at both 1338 and 1571 cm^{-1} decreased progressively with the concomitant emergence of a new Raman peak at 1590 cm^{-1}, which was assigned to 4-aminothiophenol (4-ATP).[28] The time-resolved SERS measurements also allowed us to identify 4,4′-dimercaptoazobenzene (DMAB), whose characteristic Raman modes are at 1140, 1388, and 1438 cm^{-1},[43−45] as an intermediate species formed during the reaction. The detailed assignments of the peaks observed in the SERS spectra are summarized in Table S1 in the Supporting Information. Based on the spectroscopic evolution observed in the SERS measurements, a possible reaction mechanism is proposed, which is schematically illustrated in Figure 2B. The Au NP-catalyzed hydrogenation of 4-NTP by $\mathrm{NaBH_4}$ involves three major steps: (1) generation of surface-hydrogen species upon adsorption of borohydride ions to Au surfaces; (2) reduction of surface-adsorbed 4-NTP by the surface-hydrogen species to form the intermediate, DMAB; and (3) further hydrogenation of DMAB into the final product, 4-ATP. Although similar spectral evolutions were observed on Au ETHH, TOH, and QS NPs, the reaction rates varied significantly among the Au NPs of different geometries as shown in Figures S4, S5, and S6 in the Supporting Information.

The time-resolved SERS results clearly showed that the catalytic reaction rates decreased in the order of ETHH > CC ≫ TOH > QS NPs. The facet-dependent catalytic activities observed here were intimately tied to the distribution of coordinatively unsaturated surface atoms on various facets. The atomic-level structures of {730} (ETHH NPs), {520} (CC NPs), {221} (TOH NPs), and {111} + {100} (QS NPs) facets are schematically illustrated in Figures 3A-3D, respectively, based on which the fractions of surface atoms with different coordination numbers can be calculated. We used the Raman modes at 1338 and 1590 cm^{-1} to quantify the fraction of 4-NTP and 4-ATP molecules, respectively, at various reaction times. Under our experimental conditions, $\mathrm{NaBH_4}$ (100 mM) was in excess, and its concentration maintained constant throughout the entire reaction processes. Therefore, this catalytic reaction obeyed pseudo-first-order kinetics, and the induction times and rate constants were obtained by performing least-squares curve fitting to the reactant and product trajectories shown in Figures 3E-3H. The rate equations for this two-step consecutive reaction are listed as follows

$$\theta_R = e^{-k_1 \times (t-t_0)} \tag{1}$$

$$\theta_P = 1 + \frac{(k_1 \times e^{-k_2 \times (t-t_0)} - k_2 \times e^{-k_1 \times (t-t_0)})}{k_2 - k_1} \tag{2}$$

$$\theta_I = 1 - \theta_R - \theta_P \tag{3}$$

where θ_R, θ_P, and θ_I are the fractions of 4-NTP, 4-ATP, and the intermediate (DMAB), respectively. k_1 and k_2 are the rate constants for the first and second hydrogenation steps, respectively, and t_0 is the induction time. During the catalytic reactions, successive SERS spectra were collected in real time until complete hydrogenation of 4-NTP into 4-ATP. The time resolutions of the kinetic measurements were limited by the integration times for SERS spectral collection, which were 1 s for ETHH and CC, 5 s for TOH, and 10 s for QS NPs, respectively, under the current experimental conditions. Although the excitation of plasmon resonances may enhance the rates of some catalytic surface reactions,[46,47] the catalytic 4-NTP hydrogenation was found to be neither driven by plasmons nor affected by the coupling of plasmon excitations to the reaction coordinates. The reaction rates were observed to remain essentially unchanged when various time intervals (the excitation laser was blocked by a laser beam shutter) were introduced between SERS spectral collections (Figure S7 in the Supporting Information).

In Figures 3I and 3J, we compare the rate constants and induction times on various Au NPs. The increase in rate constants was accompanied by decrease in induction times. Interestingly, the k_2 was significantly larger than k_1 on all four nanostructures, and, as a consequence, the fraction of the intermediate remained low during the reactions (see the blue dash curves in Figures 3E-3H). However, the high detection sensitivity of SERS and the large Raman cross-section of DMAB[43−45] allowed us to indentify DMAB as the intermediate and further resolve the complex kinetics of the two-step reaction. It is apparent that all the high-index facets were catalytically more active than the low-index {111} and {100} facets. The observed facet-dependent catalytic activities correlated well with the characteristic distributions of under-coordinated surface atoms on various facets as shown in Figure 3K. The {730} facets of ETHH NPs and {520} facets of CC NPs showed significantly higher catalytic activities than the {221} facets of TOH NPs because both the {730} and {520} facets have significant fraction of surface atoms with a coordination number of 6, while the lowest surface atomic coordination number on the {221} facets is 7. The {730} facets were observed to be more active than the {520} facets largely due to the higher fraction of surface atoms with coordination number of 6. In contrast, the low-index {100} and {111} facets only have surface atomic coordination numbers of 8 and 9, respectively, and thus showed much lower catalytic activities than the high-index facets.

Using this SERS-based approach to monitor the surface-catalyzed reactions has several unique advantages. Because both the reactant and product molecules were immobilized as SAMs on the nanocatalyst surfaces, it became possible to unravel the intrinsic surface reaction kinetics with minimal complication introduced by the surface-capping ligands as well as the diffusion, adsorption, and desorption of reactants and products. In addition, the catalytic reaction kinetics probed by SERS of surface-immobilized SAMs was independent of the total nanocatalyst surface areas, i.e. the concentrations of the colloidal Au NPs, in the presence of excessive $\mathrm{NaBH_4}$, which was quantitatively demonstrated on porous Au NPs in a recent publication[48] and was further verified on the Au ETHH, CC, and TOH NPs in this work (Figure S8 in the Supporting Information). This allowed us to compare the catalytic activities of various Au facets without the necessity to normalize the particle surface areas for different geometries. Furthermore, the high sensitivity and unique fingerprinting capability of SERS enabled the identification of transient intermediates along the reaction pathways. In our SERS measurements, we used a confocal Raman microscope with the laser beam focused into a small volume of the colloidal NP suspensions, and the SERS signals were collected from an observation volume of ∼100 pL. Therefore, each freely diffusing NP was exposed to the excitation laser for a short time period (within the diffusion time), effectively eliminating the plasmon-driven photoconversion of 4-NTP to DMAB[43,45] and photoinduced sample damage (see the results of control experiments in the absence of $\mathrm{NaBH_4}$ in Figures S9 and S10 in the Supporting Information). The relatively low excitation power (10.0 mW CW laser) and limited exposure time of each diffusing NP to the confocal laser beam also effectively minimized photothermal effects and suppressed other possible plasmon-enhanced surface reactions, allowing one to precisely measure the intrinsic kinetics of the catalytic chemical transformations occurring at the NP-molecule interfaces.

Our results provide clear experimental evidence on the critical contribution of undercoordinated surface atoms to the catalytic activities of Au NPs. The quantitative insights on the intrinsic facet-dependent catalytic activities of Au NPs gained through this work provide important information that guides the rational design and construction of nanoarchitectured Au surfaces for the optimization of heterogeneous catalysis.

■ ASSOCIATED CONTENT

Ⓢ Supporting Information

Experimental details, additional TEM images of individual Au ETHH, CC, and TOH NPs with different orientations, time-resolved SERS results obtained from 4-NTP-coated Au ETHH, TOH, QS NPs upon exposure to 100 mM NaBH$_4$, kinetic results obtained from SERS measurements with various time intervals between spectral collections, the effects of NP concentrations on the catalytic reaction kinetics, SERS results obtained from 4-NTP-coated Au CC and ETHH NPs in the absence of NaBH$_4$, and a table listing detailed assignments of the major peaks in the SERS spectra. This material is available free of charge via the Internet at http://pubs.acs.org.

■ AUTHOR INFORMATION

Corresponding Author

*Phone: 803-777-2203. Fax: 803-777-9521. E-mail: wang344@mailbox.sc.edu.

Notes

The authors declare no competing financial interest.

■ ACKNOWLEDGMENTS

This work was supported by the National Science Foundation through a CAREER Award (DMR-1253231) and by the University of South Carolina Office of Vice President for Research through an ASPIRE-I Track-I Award. The authors thank the University of South Carolina Electron Microscopy Center for instrument use and technical assistance.

■ REFERENCES

(1) Haruta, M.; Date, M. *Appl. Catal., A* **2001**, *222*, 427−437.

(2) Ishida, T.; Haruta, M. *Angew. Chem., Int. Ed.* **2007**, *46*, 7154−7156.

(3) Valden, M.; Lai, X.; Goodman, D. W. *Science* **1998**, *281*, 1647−1650.

(4) Schimpf, S.; Lucas, M.; Mohr, C.; Rodemerck, U.; Bruckner, A.; Radnik, J.; Hofmeister, H.; Claus, P. *Catal. Today* **2002**, *72*, 63−78.

(5) Overbury, S. H.; Schwartz, V.; Mullim, D. R.; Yan, W. F.; Dai, S. *J. Catal.* **2006**, *241*, 56−65.

(6) Hvolbaek, B.; Janssens, T. V. W.; Clausen, B. S.; Falsig, H.; Christensen, C. H.; Norskov, J. K. *Nano Today* **2007**, *2*, 14−18.

(7) Hughes, M. D.; Xu, Y. J.; Jenkins, P.; McMorn, P.; Landon, P.; Enache, D. I.; Carley, A. F.; Attard, G. A.; Hutchings, G. J.; King, F.; Stitt, E. H.; Johnston, P.; Griffin, K.; Kiely, C. J. *Nature* **2005**, *437*, 1132−1135.

(8) Zanella, R.; Louis, C.; Giorgio, S.; Touroude, R. *J. Catal.* **2004**, *223*, 328−339.

(9) Chen, M. S.; Goodman, D. W. *Science* **2004**, *306*, 252−255.

(10) Green, I. X.; Tang, W. J.; Neurock, M.; Yates, J. T. *Science* **2011**, *333*, 736−739.

(11) Janssens, T. V. W.; Clausen, B. S.; Hvolbaek, B.; Falsig, H.; Christensen, C. H.; Bligaard, T.; Norskov, J. K. *Top. Catal.* **2007**, *44*, 15−26.

(12) Lemire, C.; Meyer, R.; Shaikhutdinov, S.; Freund, H. J. *Angew. Chem., Int. Ed.* **2004**, *43*, 118−121.

(13) Yim, W. L.; Nowitzki, T.; Necke, M.; Schnars, H.; Nickut, P.; Biener, J.; Biener, M. M.; Zielasek, V.; Al-Shamery, K.; Kluner, T.; Baumer, M. *J. Phys. Chem. C* **2007**, *111*, 445−451.

(14) Wittstock, A.; Zielasek, V.; Biener, J.; Friend, C. M.; Baumer, M. *Science* **2010**, *327*, 319−322.

(15) Wittstock, A.; Baumer, M. *Acc. Chem. Res.* **2014**, *47*, 731−739.

(16) Zielasek, V.; Jurgens, B.; Schulz, C.; Biener, J.; Biener, M. M.; Hamza, A. V.; Baumer, M. *Angew. Chem., Int. Ed.* **2006**, *45*, 8241−8244.

(17) Fujita, T.; Guan, P. F.; McKenna, K.; Lang, X. Y.; Hirata, A.; Zhang, L.; Tokunaga, T.; Arai, S.; Yamamoto, Y.; Tanaka, N.; Ishikawa, Y.; Asao, N.; Erlebacher, J.; Chen, M. W. *Nat. Mater.* **2012**, *11*, 775−780.

(18) van Bokhoven, J. A.; Louis, C.; T Miller, J.; Tromp, M.; Safonova, O. V.; Glatzel, P. *Angew. Chem., Int. Ed.* **2006**, *45*, 4651−4654.

(19) Molina, L. M.; Hammer, B. *Phys. Rev. Lett.* **2003**, *90*, 206102.

(20) Moskaleva, L. V.; Rohe, S.; Wittstock, A.; Zielasek, V.; Kluner, T.; Neyman, K. M.; Baumer, M. *Phys. Chem. Chem. Phys.* **2011**, *13*, 4529−4539.

(21) Tian, N.; Zhou, Z. Y.; Sun, S. G.; Ding, Y.; Wang, Z. L. *Science* **2007**, *316*, 732−735.

(22) Quan, Z. W.; Wang, Y. X.; Fang, J. Y. *Acc. Chem. Res.* **2013**, *46*, 191−202.

(23) Zhang, H.; Jin, M. S.; Xia, Y. N. *Angew. Chem., Int. Ed.* **2012**, *51*, 7656−7673.

(24) Heck, K. N.; Janesko, B. G.; Scuseria, G. E.; Halas, N. J.; Wong, M. S. *J. Am. Chem. Soc.* **2008**, *130*, 16592−16600.

(25) Joseph, V.; Engelbrekt, C.; Zhang, J. D.; Gernert, U.; Ulstrup, J.; Kneipp, J. *Angew. Chem., Int. Ed.* **2012**, *51*, 7592−7596.

(26) Xie, W.; Herrmann, C.; Kompe, K.; Haase, M.; Schlucker, S. *J. Am. Chem. Soc.* **2011**, *133*, 19302−19305.

(27) Jing, H.; Zhang, Q. F.; Large, N.; Yu, C. M.; Blom, D. A.; Nordlander, P.; Wang, H. *Nano Lett.* **2014**, *14*, 3674−3682.

(28) Huang, J. F.; Zhu, Y. H.; Lin, M.; Wang, Q. X.; Zhao, L.; Yang, Y.; Yao, K. X.; Han, Y. *J. Am. Chem. Soc.* **2013**, *135*, 8552−8561.

(29) Chiu, C. Y.; Chung, P. J.; Lao, K. U.; Liao, C. W.; Huang, M. H. *J. Phys. Chem. C* **2012**, *116*, 23757−23763.

(30) Yu, Y.; Zhang, Q. B.; Lu, X. M.; Lee, J. Y. *J. Phys. Chem. C* **2010**, *114*, 11119−11126.

(31) Ming, T.; Feng, W.; Tang, Q.; Wang, F.; Sun, L. D.; Wang, J. F.; Yan, C. H. *J. Am. Chem. Soc.* **2009**, *131*, 16350−16351.

(32) Ma, Y. Y.; Kuang, Q.; Jiang, Z. Y.; Xie, Z. X.; Huang, R. B.; Zheng, L. S. *Angew. Chem., Int. Ed.* **2008**, *47*, 8901−8904.

(33) Zhang, J.; Langille, M. R.; Personick, M. L.; Zhang, K.; Li, S. Y.; Mirkin, C. A. *J. Am. Chem. Soc.* **2010**, *132*, 14012−14014.

(34) Hong, J. W.; Lee, S. U.; Lee, Y. W.; Han, S. W. *J. Am. Chem. Soc.* **2012**, *134*, 4565−4568.

(35) McFarland, A. D.; Young, M. A.; Dieringer, J. A.; Van Duyne, R. P. *J. Phys. Chem. B* **2005**, *109*, 11279−11285.

(36) Zuloaga, J.; Nordlander, P. *Nano Lett.* **2011**, *11*, 1280−1283.

(37) Menzel, C.; Hebestreit, E.; Muhlig, S.; Rockstuhl, C.; Burger, S.; Lederer, F.; Pertsch, T. *Opt. Express* **2014**, *22*, 9971−9982.

(38) Moreno, F.; Albella, P.; Nieto-Vesperinas, M. *Langmuir* **2013**, *29*, 6715−6721.

(39) Alonso-Gonzalez, P.; Albella, P.; Neubrech, F.; Huck, C.; Chen, J.; Golmar, F.; Casanova, F.; Hueso, L. E.; Pucci, A.; Aizpurua, J.; Hillenbrand, R. *Phys. Rev. Lett.* **2013**, *110*, 203902.

(40) Sivapalan, S. T.; DeVetter, B. M.; Yang, T. K.; van Dijk, T.; Schulmerich, M. V.; Carney, P. S.; Bhargava, R.; Murphy, C. J. *ACS Nano* **2013**, *7*, 2099−2105.

(41) Wang, H.; Halas, N. J. *Adv. Mater.* **2008**, *20*, 820−825.

(42) Herves, P.; Perez-Lorenzo, M.; Liz-Marzan, L. M.; Dzubiella, J.; Lu, Y.; Ballauff, M. *Chem. Soc. Rev.* **2012**, *41*, 5577−5587.

(43) Dong, B.; Fang, Y. R.; Chen, X. W.; Xu, H. X.; Sun, M. T. *Langmuir* **2011**, *27*, 10677−10682.

(44) Huang, Y. F.; Zhu, H. P.; Liu, G. K.; Wu, D. Y.; Ren, B.; Tian, Z. Q. *J. Am. Chem. Soc.* **2010**, *132*, 9244−9246.

(45) Sun, M. T.; Xu, H. X. *Small* **2012**, *8*, 2777−2786.

(46) Christopher, P.; Xin, H. L.; Linic, S. *Nat. Chem.* **2011**, *3*, 467−472.

(47) Kale, M. J.; Avanesian, T.; Christopher, P. *ACS Catal.* **2014**, *4*, 116−128.

(48) Zhang, Q.; Blom, D. A.; Wang, H. *Chem. Mater.* **2014**, *26*, 5131−5142.